

Research Paper

# On the Energy Storage Capacity and Design Optimization of Compound Flywheel Rotors with Prestressed Hyperbolic Disks

Sutham Arun<sup>1</sup>, Wichaphon Fakkaew<sup>1</sup>, Chakkapong Chamroon<sup>2</sup>, Matthew Owen Thomas Cole<sup>2</sup>

<sup>1</sup> School of Engineering, University of Phayao, Phayao, 56000, Thailand, Email: sutham.ar@up.ac.th (S.A.); wichaphon.fa@up.ac.th (W.F.)

<sup>2</sup> Department of Mechanical Engineering, Chiang Mai University, Chiang Mai, 50200, Thailand, Email: chakkapong@cmu.ac.th (C.C.); motcole@dome.eng.cmu.ac.th (M.O.T.C.)

Received January 08 2024; Revised April 10 2024; Accepted for publication April 13 2024.

Corresponding author: M.O.T. Cole (motcole@dome.eng.cmu.ac.th)

© 2024 Published by Shahid Chamran University of Ahvaz

**Abstract.** Flywheels used for energy storage may be assembled by press fitting or bonding of concentric rotor parts. During operation each part is subjected to a superposition of stress fields associated with centrifugal loading and with contact at the component interfaces. To capture the highest overall energy storage capacity, design properties must be selected to achieve the maximum moment of inertia, subject to constraints on the stress occurring within each part at the maximum operating speed. This paper proposes a mathematical formulation for parametric shape optimization problems which can be used to design a multi-disk flywheel rotor to maximize the energy storage capacity. It is shown that the energy storage function for each part of the flywheel can be expressed as a product of two fundamental shape-factors: one that accounts for the stress distribution and the other accounts for the mass distribution. These factors are expressed analytically for cases involving hyperbolic disks, leading to a finite dimension shape optimization problem for a multi-disk rotor. Case studies are presented based on the derived analytical solutions that show how the theory can be usefully applied in flywheel design optimization problems. The results from the case study show significant improvements in specific energy compared to previous research results. This advancement is particularly relevant to develop high-performance, cost-effective flywheel systems, offering potential for widespread application in energy storage technologies.

**Keywords:** Compound rotor, Hyperbolic disk, Shape optimization, Stress analysis, Energy storage, Specific energy.

## 1. Introduction

Flywheel energy storage systems (FESS) are being increasingly utilized in applications that require high power transfer over short time-scales – typically involving charge/discharge cycles of a few second to a few minutes [1]. Key advantages of FESS are their low degradation from cycling, low maintenance, long lifespan, and high efficiency [2, 3]. They can also be made from materials that are abundant and have low environmental impact. The main disadvantages of FESS, however, are their high cost and relatively low energy density compared with other leading technologies. This can be partly attributed to their complicated and heavy auxiliary equipment [4]. Current applications of FESS include spacecraft systems, back-up power supplies, energy recovery systems, and power grid stabilization [5].

The design optimization of flywheel structures may be considered with various objectives, such as maximizing energy density (either per unit volume or unit mass), maximizing power density, or minimizing manufacturing cost per unit of energy capacity [6, 7]. For many ground-based applications, manufacturing cost is a dominant consideration and inevitably compels the use of cheaper, less exotic materials and more cost-effective manufacturing methods. This motivates the analysis and optimization of kinetic energy storage in simple homogenous rotor parts that can be easily assembled by processes such as press fitting, bonding or friction welding.

A high-speed FESS is typically composed of a flywheel rotor, motor/generator, magnetic bearings, vacuum housing, and power transformation electronics, and has a structure similar to that shown in Fig. 1 [3, 8]. One key area for research is the design of flywheel rotors to achieve the maximum energy storage subject to safe long-term operation. This usually starts with the formulation of an objective function such as the kinetic energy  $E_k$ , the specific energy  $e_m$  or energy density  $e_v$  at the maximum operating speed [9-11]. The maximization of this function is achieved subject to stress limits for failure avoidance using appropriate mathematical optimization methods. In general terms, the energy storage capacity of the flywheel is dependent on two main properties, which are the strength-to-density ratio of the material, and the flywheel geometry [12].



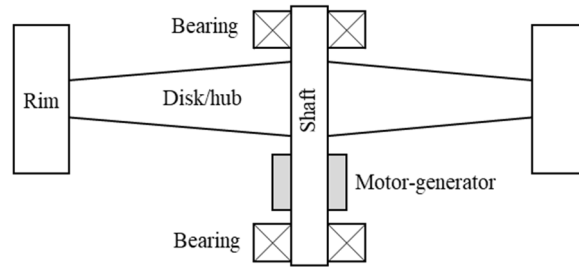


Fig. 1. Flywheel design having shaft-hub-rim structure: cross-section.

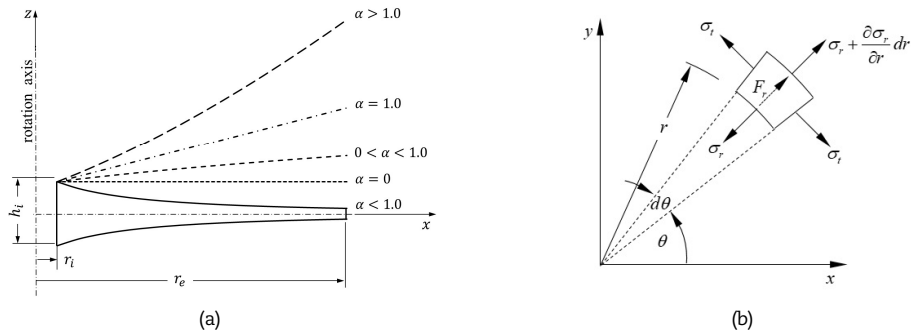


Fig. 2. (a) Hyperbolic disk profiles obtained by varying the exponent  $\alpha$  and (b) stress element in polar coordinates.

Quantifying the effects of rotor geometry on energy capacity can be challenging. For rotors made of isotropic materials, a dimensionless parameter known as the shape factor may be considered to compare different candidate geometries [13]. The shape factor  $K$ , which is commonly defined as the energy density of the rotor divided by the material's strength-to-density ratio, indicates how effectively a rotor utilizes the energy storage capability of the material used in its construction [14, 15]. To obtain high values of  $K$ , the stress within the flywheel due to rotation must be distributed as uniformly as possible so that the rotor is close to fully stressed at the point of failure. For this reason, some researchers have formulated the shape optimization problem in terms of minimizing the variation in rotor stress about a mean value [16].

For rotors made from several different materials that form concentric cylinders, the material distribution will determine the pattern of stress within the rotor, and careful sequencing of materials and layer thicknesses can bring each layer of the rotor closer to a fully stressed state at the point of failure [9, 14]. Although this method produces residual stress inside the rotor due to interference fitting of layers of material over each other, it can help designers achieve higher energy densities with their flywheels, especially when high strength orthotropic materials such as carbon composites are used [9].

This paper introduces a novel design optimization framework for energy storage flywheels composed of several concentric, non-uniform disks. The aim of the optimization problem is to maximize the energy storage capacity of a multi-disk flywheel rotor. To address this problem, an objective function is introduced that involves two distinct shape factors for each disk segment: one factor for stress distribution and another for mass distribution. These factors are pivotal in formulating a constrained optimization problem aimed at maximizing the flywheel's total energy storage, under given operational speed constraints. Case studies are included to demonstrate the application of the methodology in designing single-disk and two-disk hyperbolic flywheels. The proposed approach offers significant advancements in flywheel design to achieve higher energy storage efficiencies. The work is particularly relevant for the development of high-performance flywheel systems utilizing cost-effective materials and manufacturing methods.

The remainder of the paper is organized into three main sections: Section 2 describes the stress analysis problem for a prestressed hyperbolic rotating disk, including a treatment of energy storage capacity. The key geometric factors for the shape optimization problem are also defined in closed form. Section 3 introduces the general shape optimization problem for a compound flywheel rotor. Section 4 describes numerical case studies involving a two-part flywheel with hyperbolic disks, followed by design verification results based on finite element analysis. The final section provides conclusions.

## 2. Energy Storage Capacity of Prestressed Hyperbolic Disks

A hyperbolic annular disk geometry can be usefully considered for rotor design optimization problems as it may represent various types of disk profile, as illustrated in Fig. 2. The disk thickness  $h$  may be expressed as a function of radius according to [17, 18]:

$$h(\rho) = h_i \left( \frac{\rho}{\beta} \right)^\alpha \quad (1)$$

where  $\rho = r/r_e$  is the radial distance as a fraction of the outer radius  $r_e$ , and  $\beta = r_i/r_e$  is the ratio of inner and outer radius. The hyperbolic function can represent a constant thickness disk ( $\alpha = 0$ ), a disk profile that tapers nonlinearly from the inner to the outer radius ( $\alpha < 0$ ), and a disk profile that diverges from the inner to the outer radius, both nonlinearly ( $\alpha > 0$ ) and linearly ( $\alpha = 1$ ). Also important, is that the hyperbolic function admits analytical solution of the stress field equations under some standard simplifying assumptions. In this work, a flywheel formed from disks that are assembled concentrically by bonding or press/shrink fitting is considered. Therefore, the interfacial stress that arises at the inner and outer circumferential surfaces must be accounted for in the analysis, as depicted in Fig. 3.



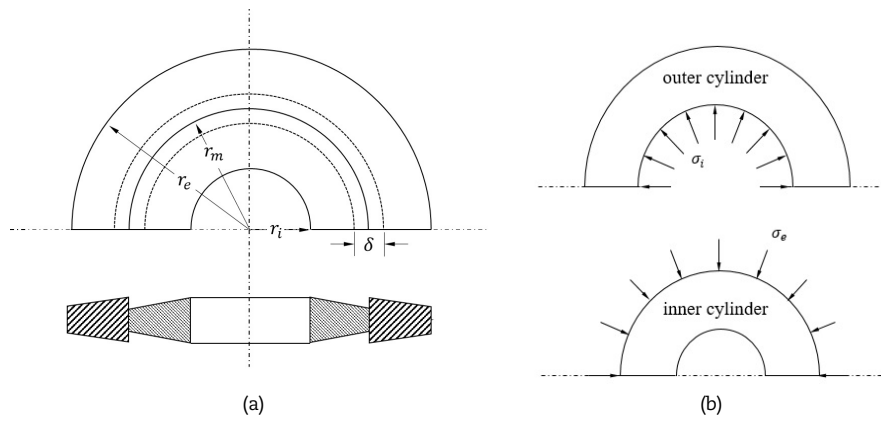


Fig. 3. (a) Compound cylinder after assembly and (b) the interfacial stress due to press fitting.

## 2.1. Stress solution

The basic theory for calculating the stress distribution of an isotropic rotor subjected to centrifugal forces has been published previously in the literature [18, 19]. By considering the stresses on a typical infinitesimal element within the rotating disk (Fig. 2b), together with the conditions of symmetry, the differential equation describing the radial displacement field  $u(r)$  can be derived as:

$$\frac{d^2u}{dr^2} + \left( \frac{1}{h} \frac{dh}{dr} + \frac{1}{r} \right) \frac{du}{dr} + \left( \frac{\nu}{hr} \frac{dh}{dr} - \frac{1}{r^2} \right) u + (1-\nu^2) \frac{\gamma \omega^2 r}{E} = 0 \quad (2)$$

Here,  $E$  and  $\nu$  are the material Young's modulus and Poisson's ratio respectively,  $\gamma$  is the material density, and  $\omega$  is the rotational speed. This equation is derived under the assumptions that the material has isotropic linear elastic properties, and that the displacement field is independent of axial position. The radial and tangential stress can be related to the radial displacement  $u$  by the following equations:

$$\sigma_r = \frac{E}{1-\nu^2} \left( \frac{du}{dr} + \nu \frac{u}{r} \right) \quad (3)$$

$$\sigma_t = \frac{E}{1-\nu^2} \left( \frac{u}{r} + \nu \frac{du}{dr} \right) \quad (4)$$

Introducing the expression of  $h$  given by Eq. (1) in Eq. (2), yields the following differential equation for the displacement field of a hyperbolic disk:

$$\frac{d^2u}{dr^2} + \left( \frac{\alpha+1}{\rho} \right) \frac{du}{d\rho} + (\nu\alpha-1) \frac{u}{\rho^2} + \frac{(1-\nu^2)\gamma\omega^2 r_e^3 \rho}{E} = 0 \quad (5)$$

This has the form of a 2<sup>nd</sup> order linear differential equation with non-constant coefficients, the complete solution for which has the form:

$$u = C_1 \rho^p + C_2 \rho^q - \frac{(1-\nu^2)\gamma\omega^2 r_e^3}{E[8+(3+\nu)\alpha]} \rho^3 = 0 \quad (6)$$

where  $C_1$  and  $C_2$  are integration constants and:

$$p = -\frac{\alpha}{2} + \sqrt{1-\nu\alpha + \frac{\alpha^2}{4}} \quad \text{and} \quad q = -\frac{\alpha}{2} - \sqrt{1-\nu\alpha + \frac{\alpha^2}{4}} \quad (7)$$

Inserting Eq. (6) into Eqs. (3) and (4), the expressions for radial and circumferential stress are obtained in the form:

$$\sigma_r = A \rho^{p-1} + B \rho^{q-1} - C \rho^2 \quad (8)$$

$$\sigma_t = -qA \rho^{p-1} + pB \rho^{q-1} - D \rho^2 \quad (9)$$

The constants  $C$  and  $D$  are known terms that depend on  $\sigma_o = \gamma \omega^2 r_e^2$  according to:

$$C = \frac{(3+\nu)}{[8+(3+\nu)\alpha]} \sigma_o \quad \text{and} \quad D = \frac{(1+3\nu)}{[8+(3+\nu)\alpha]} \sigma_o \quad (10)$$

The other integration constants  $A$  and  $B$  can be evaluated from the boundary conditions, as given by  $(\sigma_r)_{\rho=\beta} = \sigma_i$  and  $(\sigma_r)_{\rho=1} = \sigma_e$ , yielding:



$$A = \frac{1}{(\beta^{p-1} - \beta^{q-1})} [C(\beta^2 - \beta^{q-1}) - \sigma_e \beta^{q-1} + \sigma_i] \tag{11}$$

$$B = \frac{1}{(\beta^{p-1} - \beta^{q-1})} [-C(\beta^2 - \beta^{p-1}) + \sigma_e \beta^{p-1} + \sigma_i] \tag{12}$$

The radial displacement  $u$  is related to the stresses according to:

$$u = \frac{r}{E} [\sigma_t - \nu \sigma_r] \tag{13}$$

Introducing Eqs. (8)-(12) into Eq. (13), the radial displacement is expressed as a function of  $\rho$ :

$$u = \frac{r_e}{E} \rho [-(q + \nu)A \rho^{p-1} - (p + \nu)B \rho^{q-1} - (D - \nu C)\rho^2] \tag{14}$$

Substituting Eqs. (11) and (12) into Eqs. (8), (9) and (14), provides the following expressions:

$$\sigma_r = (\sigma_r)_\omega + (\sigma_r)_e + (\sigma_r)_i \tag{15}$$

$$\sigma_t = (\sigma_t)_\omega + (\sigma_t)_e + (\sigma_t)_i \tag{16}$$

$$u_r = u_\omega + u_e + u_i \tag{17}$$

where the subscripts  $\omega$ ,  $e$  and  $i$  denote the components associated with  $\sigma_\omega$ ,  $\sigma_e$  and  $\sigma_i$ , respectively. The expressions for each component on the right-hand side of Eqs. (15), (16) and (17) are presented in the Appendix.

### 2.2. Maximum permitted angular velocity

In practice, the maximum rotational speed will be limited by the maximum allowed stress. According to Tresca's yield condition, plastic deformation will occur if [20-22]:

$$\sigma_{\max} - \sigma_{\min} \geq \sigma_y$$

Tresca's condition has the advantage of being a linear constraint, and is also more conservative than the commonly used von Mises criterion. The left-hand side of the above equation represents the Tresca equivalent stress, defined as the difference between the maximum principal stress  $\sigma_{\max}$  and the minimum principal stress  $\sigma_{\min}$ , and  $\sigma_y$  denotes the initial tensile yield stress. For the case of a hyperbolic disk with  $\alpha \geq 0$ , the maximum value of the Tresca stress will occur at the inner surface of the disk ( $\rho = \beta$ ) when operating at high rotational speeds. Since  $\sigma_t$  is positive and  $\sigma_r$  is negative (or zero) at the inner surface, Tresca's condition to avoid yielding then takes the form:

$$(\sigma_t)_{\rho=\beta} - (\sigma_r)_{\rho=\beta} \leq \sigma_y \tag{18}$$

For some cases with  $\alpha < 0$ , it is possible that the maximum shear stress occurs away from the inner surface of the disk so that Eq. (18) is no longer applicable. This tends to occur only for small values of  $\beta$ . In general, the applicability of Eq. (18) is dependent on the values of  $\beta$  and  $\alpha$ , as shown in Fig. 4 for the case of a rotating hyperbolic disk without preload and rotating disk loaded at the outer surface only ( $\sigma_e/\sigma_\omega = 0.1$ ).

Using Eqs. (15) and (16) in Eq. (18) leads to:

$$\sigma_\omega < \kappa_\omega (\sigma^{\text{lim}} - c_e \sigma_e + c_i \sigma_i) \tag{19}$$

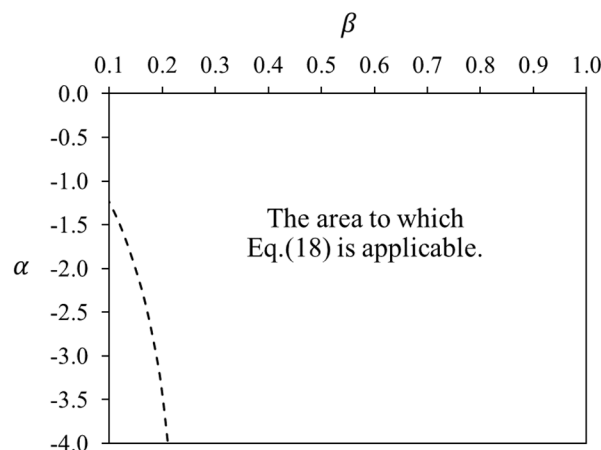


Fig. 4. Set of parameter values where the failure criterion Eq. (18) is applicable.



where  $\sigma^{\text{lim}}$  is the maximum allowed stress value. This may be computed by dividing  $\sigma_y$  by a suitable factor of safety for the flywheel [23], and:

$$\kappa_\omega = \frac{[8 + (3 + \nu)\alpha](\beta^p - \beta^q)\beta}{(q - p)(3 + \nu)\beta^{p+q} - [1 + 3\nu + q(3 + \nu)]\beta^{p+3} + [1 + 3\nu + p(3 + \nu)]\beta^{q+3}} \quad (20)$$

$$c_e = \frac{(q - p)\beta^{p+q-1}}{\beta^p - \beta^q} \quad (21)$$

$$c_i = 1 - \frac{p\beta^q - q\beta^p}{\beta^p - \beta^q} \quad (22)$$

It can be seen that  $\kappa_\omega$ ,  $c_e$  and  $c_i$  are dimensionless shape factors that capture how the Tresca stress is affected by the centrifugal force, external pressure and internal pressure, respectively. Equation (19) may be rearranged to obtain:

$$\omega \leq \bar{\omega} := \frac{1}{r_e} \sqrt{\frac{\kappa_\omega^\sigma \sigma^{\text{lim}}}{\gamma}} \quad (23)$$

where

$$\kappa_\omega^\sigma(\alpha, \beta) = \kappa_\omega(\alpha, \beta) \left[ 1 - c_e(\alpha, \beta) \left( \frac{\sigma_e}{\sigma^{\text{lim}}} \right) + c_i(\alpha, \beta) \left( \frac{\sigma_i}{\sigma^{\text{lim}}} \right) \right] \quad (24)$$

Figure 5 shows the values of  $\kappa_\omega$ ,  $c_e$  and  $c_i$  as a function of the radius ratio  $\beta$  for selected disk profiles (values of  $\alpha$ ). It is seen that, for a relatively thin ring ( $\beta > 0.8$ ), the values of  $\kappa_\omega$  are close to 1 for all profiles. The figure also shows that the values of  $c_e$  and  $c_i$  are always positive. As a consequence, applying pressure on the outer surface (so that  $\sigma_e$  is negative) causes the maximum angular velocity  $\bar{\omega}$  to increase. Applying pressure  $\sigma_i$  on the inner surface, on the other hand, reduces the maximum angular velocity. For tensile loading, these effects are reversed.

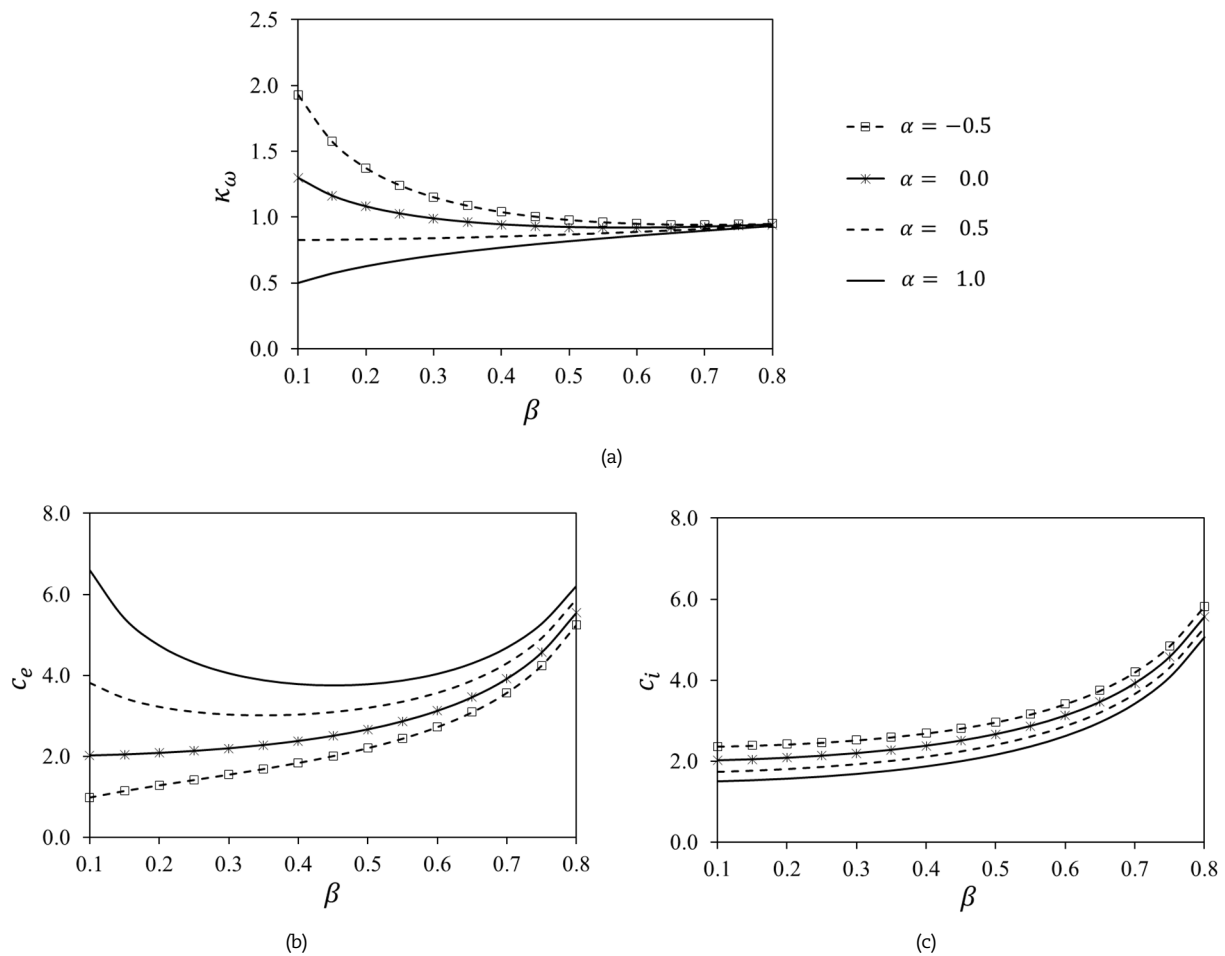


Fig. 5. The values of  $\kappa_\omega$ ,  $c_e$  and  $c_i$  for general metals ( $\nu = 0.3$ ).



**Table 1.** Shape factors for some common rotor geometries.

Geometry	$\alpha$	$\beta$	Shape factor (K)
Constant stress disk, theoretical (Laval)	-	-	1.000
Constant stress disk, practical [14]	-	-	0.645
Constant thickness solid disk	-	-	0.606
Thin annular ring	0.00	0.999	0.500
Uniform annular disk	0.00	0.200	0.313
Hyperbolic annular disk (converging)	-1.00	0.200	0.440
Hyperbolic annular disk (diverging)	1.00	0.200	0.222

### 2.3. Energy storage capacity

The mass moment of inertia for a hyperbolic disk, can be expressed in the form:

$$J = V \gamma \kappa^J(\alpha, \beta) r_e^2 \quad (25)$$

where  $V$  is the volume and the factor  $\kappa^J$  captures the mass distribution of the disk:

$$\kappa^J(\alpha, \beta) = \left( \frac{\alpha + 2}{\alpha + 4} \right) \left( \frac{1 - \beta^{\alpha+4}}{1 - \beta^{\alpha+2}} \right) \quad (26)$$

Using the maximum permitted value of rotational speed defined by Eq. (23), the energy storage capacity of the disk is obtained as:

$$\bar{E}_k = \frac{1}{2} J \bar{\omega}^2 = \frac{1}{2} V \gamma \kappa^J(\alpha, \beta) \kappa^\sigma(\alpha, \beta) \sigma^{\text{lim}}$$

Hence, the specific energy capacity of a prestressed hyperbolic disk is:

$$e_m = \frac{\bar{E}_k}{\gamma V} = K(\alpha, \beta) \frac{\sigma^{\text{lim}}}{\gamma} \quad (27)$$

where

$$K(\alpha, \beta) = \frac{1}{2} \kappa^J(\alpha, \beta) \kappa^\sigma(\alpha, \beta) \quad (28)$$

According to Eq. (28), the flywheel shape factor (as conventional defined [7, 9, 14]) may be further factorized into two shape factors that account separately for the mass distribution and stress distribution occurring within the structure.

To make the best use of a given amount of any material, the overall shape factor  $K$  must be maximized. Equation (27) also indicates that, to obtain high specific energy, flywheel materials should have a high ratio of tensile strength to density ( $\sigma^{\text{lim}} / \gamma$ ). According to Eq. (23), this will also result in high rotational speeds. Modern composite materials can have higher strength-to-weight ratio compared with metals. However, the cost of metals is typically 20-30 times lower than those of composite materials [24]. Also, manufacturing and assembly processes are much simpler. An additional consideration is whether the required rotational speeds for maximum utilization are practical for the overall design and operation of the FESS, and in some design cases the maximum speed may be fixed a-priori. These same issues are involved in the design of compound flywheel rotors, although their analysis and solutions become more complex.

The problem of maximizing the energy storage capacity of a rotor through shape optimization can be defined for two distinct cases: Case 1, with the maximum rotational speed  $\bar{\omega}$  unspecified; and Case 2 with the maximum rotational speed taking a pre-specified value  $\bar{\omega} = \omega_d$ . For the single-disk rotor, these may be defined as follows:

*Case 1:  $\bar{\omega}$  free*

For a single-disk rotor, the shape giving the highest specific energy capacity is obtained by maximizing  $K(\alpha, \beta)$  over  $\alpha$  and  $\beta$ . The theoretical upper limit for  $K$  is 1, which is achieved only for the uniform strength (Laval) disk having a Gaussian profile of infinite radius [25, 26]. The shape factors of some common practical geometries are presented in Table 1. It should be recognized here that the value of the shape factor also depends on the adopted failure criterion.

*Case 2:  $\bar{\omega}$  fixed*

The rotational kinetic energy of the disk at a prescribed maximum speed  $\bar{\omega} = \omega_d$  can be expressed:

$$\bar{E}_k = \frac{1}{2} V \gamma \kappa^J(\alpha, \beta) r_e^2 \omega_d^2$$

where the stress limit defined by Eq. (23) implies that  $\gamma r_e^2 \omega_d^2 \leq \kappa^\sigma(\alpha, \beta) \sigma^{\text{lim}}$  must also hold. Accordingly, optimization of the specific energy capacity involves solving the following problem:

$$\text{Maximize } e_m = \frac{1}{2} \kappa^J(\alpha, \beta) r_e^2 \omega_d^2 \quad \text{subject to } \kappa^\sigma(\alpha, \beta) \sigma^{\text{lim}} \geq \gamma r_e^2 \omega_d^2$$

This problem involves not only the dimensionless shape parameters but also the peripheral velocity  $r_e \omega_d$  and material



properties. The optimized value of  $\kappa^J$  may be higher than for Case 1, but the product  $\kappa^J \kappa^\sigma$  will always be lower.

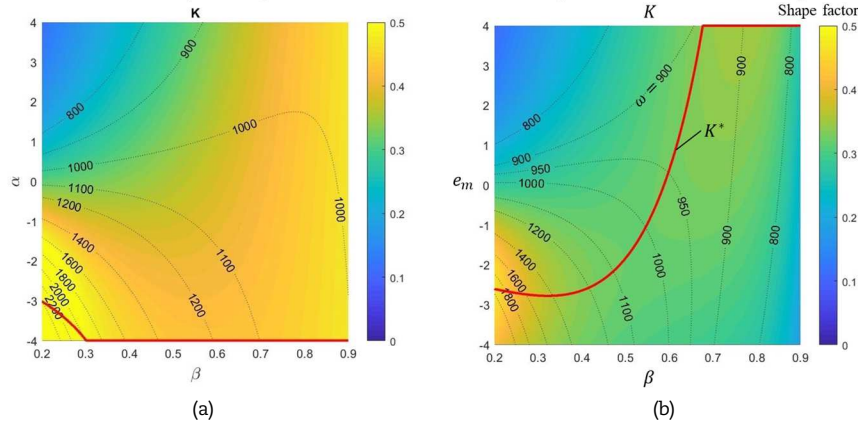


Fig. 6. Values of shape factor  $K$  and maximum rotational speeds for an annular hyperbolic disk (a) without preload and (b) with internal preload ( $\sigma_i = -23.5$  MPa).

Figure 6 shows the contour plot of the overall shape factor  $K$  and maximum speed  $\bar{\omega}$  for various values of  $\alpha$  and  $\beta$ . The rotational speed values are based on the material properties for steel-4340 and an outer radius of  $r_e = 250$  mm. The figure also shows the optimal values of  $\alpha$  and  $\beta$  which can yield the highest value of  $K$  for different rotational speeds (shown by  $K^*$ ). It can be seen that, with preload, the optimal profile varies from converging ( $\alpha < 0$ ) to diverging ( $\alpha > 0$ ), depending on the value of  $\beta$ .

### 3. Compound Flywheel Optimization Problem

For a rotor that is assembled from multiple components, here indexed by  $n$ , the total kinetic energy may be expressed:

$$E_k = \frac{1}{2} \sum_n J_n \omega_n^2 V \quad (29)$$

The moment of inertia  $J_n$  of each part depends on a set of dimensionless geometric parameters  $p_n$  (as shown for the hyperbolic disk by Eq. (25)):

$$J_n = V_n \gamma_n \kappa_n^J(p_n) r_n^2 \quad (30)$$

In this equation,  $\gamma_n$  is the material density,  $V_n$  is the volume and  $r_n$  is a characteristic radius (such as the inner or outer radius). The peak stress occurring within the part due to the combination of centrifugal loading and component interactions may be expressed:

$$\bar{\sigma}_n = \gamma_n \kappa_n^\sigma(p_n) r_n^2 \omega^2 \quad (31)$$

where the dimensionless factor  $\kappa_n^\sigma(p_n)$  can be determined through calculation of the internal stress distribution, as shown analytically for the hyperbolic disk in section 2.1. In general, for optimization purposes, this factor must be treated as a (possibly non-smooth) function of the shape parameters  $p_n$ .

Note that the dimensionless factor  $\kappa_n^\sigma(p_n)$  is also dependent on the component interaction pressures at the inner and outer surfaces, as shown for the hyperbolic disk by Eq. (24). In reality, these pressures will vary with rotational speed. However, for optimization purposes, the interaction pressures can be set to fixed values in the stress calculation. These prescribed contact pressures can always be achieved at the maximum operating speed by manufacture and assembly of the rotor components with the correct amount of radial interference.

Given that the allowed operation is constrained by  $\bar{\sigma}_n < \sigma_n^{\text{lim}}$  over all parts, the maximum rotational speed  $\bar{\omega}$  for the compound rotor must be set according to:

$$\bar{\omega}^2 = \min_n \bar{\omega}_n^2 = \min_n \left( \frac{\kappa_n^\sigma(p_n) \sigma_n^{\text{lim}}}{\gamma_n r_n^2} \right) \quad (32)$$

Based on Eqs. (29), (30) and (32), the problem of maximizing the energy storage capacity through shape optimization of each part can be defined as follows:

Case 1:  $\bar{\omega}$  free

$$\begin{aligned} \text{Maximize } \bar{E}_k &= \frac{1}{2} \min_j \left( \frac{\kappa_j^\sigma(p_j) \sigma_j^{\text{lim}}}{\gamma_j r_j^2} \right) \sum_n V_n \gamma_n \kappa_n^J(p_n) r_n^2 \\ \text{over } p_n &\in \Gamma_n, \quad n = 1, \dots, N \end{aligned} \quad (33)$$

Case 2:  $\bar{\omega}$  fixed

$$\text{Maximize } \bar{E}_k = \frac{1}{2} \omega_d^2 \sum_n V_n \gamma_n \kappa_n^J(p_n) r_n^2 \quad \text{subject to} \quad \frac{\kappa_n^\sigma(p_n) \sigma_n^{\text{lim}}}{\gamma_n r_n^2} \geq \omega_d^2 \quad (34)$$



over  $p_n \in \Gamma_n$ ,  $n = 1, \dots, N$

**Table 2.** Data for flywheel designs from the case studies conducted by Kale and Secanell [9].

Material	E (GPa)	$\nu$ (GPa)	$\gamma$ (kg/m <sup>3</sup> )	Yield strength (MPa)	$\omega_d$ (rad/s)	Kinetic energy (kJ)	Mass (kg)	$e_m$ (kJ/kg)
Carbon-Steel-1020	206.2	0.288	7 840	429.6	1 238	685.47	34.35	19.96
Steel-4340	205.0	0.29	7 850	470	1 293	749.61	34.40	21.79
Steel-18Ni-300	190.0	0.318	8 040	758	1 619	1203.03	35.23	34.15
Stainless-Steel-15-7	201.0	0.32	7 670	745	1 642	1180.8	33.61	35.13
Al-6061-T6	69.6	0.331	2 710	275	1 645	418.86	11.87	35.29
Al-2024	73.1	0.332	2 770	417.8	2 007	637.04	12.13	52.52
Stainless-Steel-440C	203.0	0.284	7 700	1220	2 105	1947.44	33.74	57.72
Al-7075-T6	71.8	0.33	2 790	465	2 111	709.56	12.22	58.07
Stainless-Steel-455	197.9	0.3	7 760	1489	2 313	2369.82	34.00	69.7

In both these cases,  $\Gamma_n$  denotes the constraint set for the geometric parameters that define the shape of the  $n^{\text{th}}$  part. In general, the utilization of global non-smooth optimization techniques will be required to solve these types of problem.

A fundamental property of the optimal solutions is that all the rotor parts must have the same maximum rotational speed. This can be seen from Eq. (33) because, if the value of  $\bar{\omega}_i$  for some part  $i$  is greater than the minimum value over all parts ( $\bar{\omega}_i > \min \bar{\omega}_n$ ), there will be remaining design freedom that can be used to increase the corresponding value of  $\kappa_i^J$  (assuming no other design constraints are active), and thereby increase  $\bar{E}_k$ . Consequently, the optimal solution must involve  $\bar{\omega}_1^2 = \bar{\omega}_2^2 = \dots = \bar{\omega}_N^2$  and the kinetic energy can then be expressed:

$$\bar{E}_k = \frac{1}{2} \sum_n V_n \kappa_n^J(p_n) \kappa_n^\sigma(p_n) \sigma_n^{\text{lim}} = \frac{1}{2} \sum_n m_n \kappa_n^J(p_n) \kappa_n^\sigma(p_n) \frac{\sigma_n^{\text{lim}}}{\gamma_n} \quad (35)$$

This also gives the specific energy of the rotor in the form:

$$e_m = \frac{\bar{E}_k}{\sum_n m_n} = \frac{1}{\sum_n m_n} \sum_n m_n \kappa_n^J(p_n) \kappa_n^\sigma(p_n) \frac{\sigma_n^{\text{lim}}}{\gamma_n} \quad (36)$$

It is important to recognize that Eq. (36) cannot be considered alone to optimize the design of a compound rotor, as it is only obtained under the additional constraint  $\bar{\omega}_1^2 = \bar{\omega}_2^2 = \dots = \bar{\omega}_N^2$ .

## 4. Case Studies

The purpose of this section is to present the methodologies for applying the theory developed in this paper and to explore the potential benefits of the hyperbolic single-disk and two-disk flywheel designs. These are shown through case studies involving the same preliminary design conditions used by Kale and Secanell [9] in the optimization of single-rim metal flywheels. Their study considered uniform annular disks with fixed rotor height of 50 mm, inner radius of 110 mm and outer radius of 200 mm. The maximization of specific energy capacity was considered for various material choices, with the relevant results summarized in Table 2.

In the present study, the equations developed for the pre-stressed hyperbolic disks in section 2 are applied to obtain optimized flywheel designs having the same overall inner and outer radii. The objective of the design optimization is to maximize the value of  $e_m$ . Both single-disk and two-disk compound flywheels are considered.

### 4.1. Optimization of single-disk flywheels

The specific energy capacity of a single-disk flywheel can be obtained from Eq. (27). In this case, the values of  $r_i = 110$  mm and  $r_e = 200$  mm are already set. Therefore, the value of the variable  $\beta = r_i/r_e = 0.55$  cannot be changed. The shape optimization problems can be formulated according to the theory in section 2.3:

Case 1:  $\bar{\omega}$  free

$$\text{Maximize } f = K(\alpha) = \frac{1}{2} \kappa^J(\alpha) \kappa^\sigma(\alpha) \text{ over } \alpha \quad (37)$$

Case 2:  $\bar{\omega} = \omega_d$

$$\text{Maximize } f = \kappa^J(\alpha) \text{ over } \alpha \text{ subject to } \kappa^\sigma(\alpha) \sigma^{\text{lim}} \geq \gamma r_e^2 \omega_d^2 \quad (38)$$

### 4.2. Optimization of compound flywheels

Consider the compound flywheel, as shown in Fig. 3, with inner disk ( $n = 1$ ) and outer disk ( $n = 2$ ) where the radius at the interface is defined as  $r_m = r_{e1} = r_{i2}$ . Also, the overall inner and outer radius are  $r_i = r_{i1}$  and  $r_e = r_{e2}$ , respectively. Accordingly, the maximum kinetic energy of the flywheel follows from Eq. (35), and the previous definitions of  $\kappa^J$  and  $\kappa^\sigma$  for the hyperbolic disk:

$$\bar{E}_k = \frac{1}{2} [m_1 \kappa^J(\alpha_1, \beta_1) \beta_1^2 + m_2 \kappa^J(\alpha_2, \beta_2)] r_e^2 \bar{\omega}^2$$

where  $\beta_1 = r_i/r_m$  and  $\beta_2 = r_m/r_e$ . For the optimization cases, the fixed parameters are chosen as follows:



- The inner and the outer disk are made of the same material.
- Inner radius of inner disk ( $r_{i1}$ ) and outer radius of outer disk/rim ( $r_{e2}$ ) are fixed as  $r_{i1} = 110$  mm and  $r_{e2} = 200$  mm.
- Based on the data in [9], no pressure acts on the inner and outer surfaces of the flywheel:  $\sigma_{i1} = \sigma_{e2} = 0$ .
- The interaction pressure between the press-fitted rims of compound cylinder is set to 0.5% of yield strength at the operating speed (in practice, this value can be designed based on the initial values of radial interference in press fitting):  $\sigma_{e1} = \sigma_{i2} = -0.005 \sigma_n^{\text{lim}}$ .
- The value of mass ratio ( $\eta$ ) is set as:  $\eta = m_2/m_1 = 2$  (in the optimization process, this value must be set to control the height ratio for the outer and inner disks).

According to these specifications, the optimization will involve the three dimensionless variables  $\alpha_1$ ,  $\alpha_2$  and  $\beta_2$ . Additionally,  $\beta_1 = 0.2 \beta_2^{-1}$ . From this, the optimization problems have the following forms:

Case 1:  $\bar{\omega}$  free

$$\begin{aligned} \text{Maximize } f &= \left[ \kappa_1^J(\alpha_1, 0.2 \beta_2^{-1}) \beta_2^2 + \eta \kappa_2^J(\alpha_2, \beta_2) \right] \kappa_2^\sigma(\alpha_2, \beta_2) \quad \text{over } \alpha_1, \alpha_2, \beta_2 \\ \text{subject to } & \gamma_1 \sigma_2^{\text{lim}} \kappa_2^\sigma(\alpha_2, \beta_2) \beta_2^2 - \gamma_2 \sigma_1^{\text{lim}} \kappa_1^\sigma(\alpha_1, 0.2 \beta_2^{-1}) \leq 0 \end{aligned} \quad (39)$$

Case 2:  $\bar{\omega} = \omega_d$

$$\begin{aligned} \text{Maximize } f &= \left[ \kappa_1^J(\alpha_1, 0.2 \beta_2^{-1}) \beta_2^2 + \eta \kappa_2^J(\alpha_2, \beta_2) \right] \quad \text{over } \alpha_1, \alpha_2, \beta_2 \\ \text{subject to } & \kappa_1^\sigma(\alpha_1, 0.2 \beta_2^{-1}) \sigma_1^{\text{lim}} \geq \gamma_1 \beta_2^2 r_e^2 \omega_d^2 \quad \text{and} \quad \kappa_2^\sigma(\alpha_2, \beta_2) \sigma_2^{\text{lim}} \geq \gamma_2 r_e^2 \omega_d^2 \end{aligned} \quad (40)$$

Equation (39) is formulated for the case in which both the inner and the outer parts of the flywheel are made of the same material. However, in the case of a compound flywheel, where the inner and the outer parts are constructed from different materials, the optimization problem for maximizing the energy storage also involves the ratio of tensile strength to density, as follows:

Case 1:  $\bar{\omega}$  free

$$\begin{aligned} \text{Maximize } f &= \left[ \kappa_1^J(\alpha_1, 0.2 \beta_2^{-1}) \beta_2^2 + \eta \kappa_2^J(\alpha_2, \beta_2) \right] \kappa_2^\sigma(\alpha_2, \beta_2) \left( \frac{\sigma_2^{\text{lim}}}{\gamma_2} \right) \quad \text{over } \alpha_1, \alpha_2, \beta_2 \text{ and materials} \\ \text{subject to } & \gamma_1 \sigma_2^{\text{lim}} \kappa_2^\sigma(\alpha_2, \beta_2) \beta_2^2 - \gamma_2 \sigma_1^{\text{lim}} \kappa_1^\sigma(\alpha_1, 0.2 \beta_2^{-1}) \leq 0 \end{aligned} \quad (41)$$

### 4.3. Results and discussion

The nonlinear constrained optimization problems defined by Eqs. (37)-(40) can be solved by several methods, such as Karush-Kuhn-Tucker conditions (KKT) and genetic algorithm (GA). In this study, an evolutionary algorithm (EA) [27, 28] was chosen. This algorithm was implemented through the built-in optimization functions in MS-Excel spreadsheet software, which was found to be a straight-forward and effective choice. For the optimization, the design variables  $\alpha$  for the single disk flywheel and  $\alpha_1$ ,  $\alpha_2$  for the compound flywheel were constrained to be within the interval  $[-4.0, 4.0]$ . Referring to section 4.1 and 4.2, it is evident that the height of the flywheel ( $h$ ) is not considered as an initial condition in the optimization process as the optimization equations presented in section 2 do not incorporate height variables. However, upon obtaining the design variable from the optimization process, we can determine the suitable value of  $h$  and the profiles of the flywheel using Eq. (1). Figure 7 illustrates the procedure for determining the solutions of Eqs. (37)-(40) using an EA.

It is important to note that for certain problems, such as the compound flywheel optimization for fixed rotational speed, there will be a finite set of solutions that give objective function values very close to the optimum value. Therefore, the use of solvers with randomization, like EA, can cause variability in the optimal parameters obtained. The optimization results obtained from the EA are presented in the following subsections.



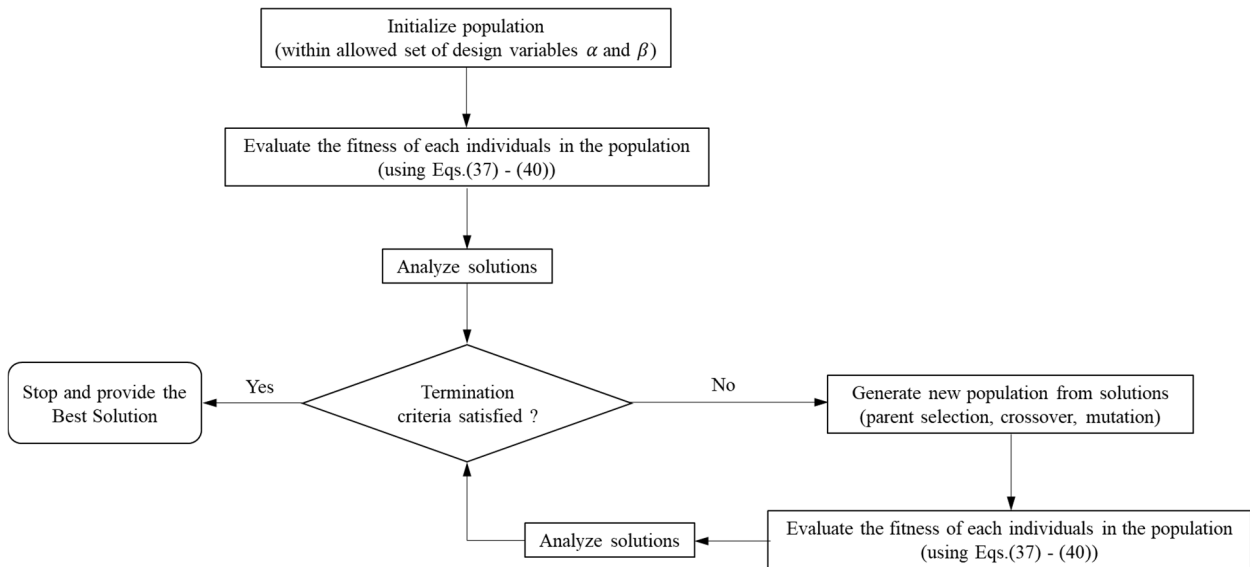


Fig. 7. Schematic of solution determination using EA.

Table 3. Optimal designs for single-disk flywheel, case 1 and case 2.

Material	Case 1: $\bar{\omega}$ free				Case 2: $\bar{\omega} = \omega_d$			
	$\omega_d$ (rad/s)	$\alpha$	$e_m$ (kJ/kg)	Difference from [9] (%)	$\omega_d$ (rad/s)	$\alpha$	$e_m$ (kJ/kg)	Difference from [9] (%)
Carbon-Steel-1020	1 498	-4.0	23.3	+14.3	1 238	0.25	20.16	+1.0
Steel-4340	1 566	-4.0	25.45	+14.4	1 293	0.25	22.02	+1.0
Steel-18Ni-300	1 962	-4.0	39.96	+14.5	1 619	0.24	34.49	+1.0
Stainless-Steel-15-7	1 992	-4.0	41.16	+14.6	1 642	0.25	35.5	+1.0
Al-6061-T6	2 035	-4.0	42.96	+17.9	1 645	0.66	36.35	+2.9
Al-2024	2 480	-4.0	63.84	+17.7	2 007	0.64	54.05	+2.8
Stainless-Steel-440C	2 584	-4.0	67.39	+14.4	2 105	0.25	58.33	+1.1
Al-7075-T6	2 608	-4.0	70.56	+17.7	2 111	0.64	59.77	+2.8
Stainless-Steel-455	2 802	-4.0	81.48	+14.5	2 313	0.25	70.42	+1.0

Table 4. Optimal designs for two-disk compound flywheel: case 1.

Material	Case 1: $\bar{\omega}$ free						
	$\alpha_1$	$\alpha_2$	$\beta_2$	$e_m$ (kJ/kg)	$\omega_1$ (rad/s)	$\omega_2$ (rad/s)	Difference from [9] (%)
Carbon-Steel-1020	4.00	4.00	0.93	22.10	1 202	1 144	+9.7
Steel-4340	4.00	4.00	0.93	24.15	1 256	1 196	+9.8
Steel-18Ni-300	4.00	4.00	0.93	37.99	1 570	1 500	+10.1
Stainless-Steel-15-7	4.00	4.00	0.93	39.13	1 592	1 522	+10.2
Al-6061-T6	4.00	4.00	0.93	40.87	1 624	1 555	+33.2
Al-2024	4.00	4.00	0.93	60.74	1 980	1 896	+13.5
Stainless-Steel-440C	4.00	4.00	0.93	63.92	2 045	1 946	+9.7
Al-7075-T6	4.00	4.00	0.93	67.13	2 082	1 993	+13.5
Stainless-Steel-455	4.00	4.00	0.93	77.37	2 245	2 141	+9.9

Table 5. Optimal designs for two-disk compound flywheel: case 2.

Material	$\omega_d$ (rad/s)	Case 2: $\bar{\omega} = \omega_d$						
		$\alpha_1$	$\alpha_2$	$\beta_2$	$e_m$ (kJ/kg)	$\omega_1$ (rad/s)	$\omega_2$ (rad/s)	Difference from [9] (%)
Carbon-Steel-1020	1 238	4.00	-2.93	0.76	20.13	1 565	1 236	+1.4
Steel-4340	1 293	4.00	-3.65	0.77	22.25	1 602	1 291	+2.1
Steel-18Ni-300	1 619	4.00	-3.88	0.77	35.10	1 988	1 616	+4.9
Stainless-Steel-15-7	1 642	4.00	-2.93	0.71	34.04	2 223	1 639	-3.2
Al-6061-T6	1 645	4.00	-0.15	0.73	35.60	2 197	1 643	+0.9
Al-2024	2 007	4.00	-3.91	0.81	57.24	2 363	2 004	+8.2
Stainless-Steel-440C	2 105	4.00	-1.75	0.73	56.66	2 780	2 101	-1.9
Al-7075-T6	2 111	4.00	-3.80	0.81	63.20	2 489	2 107	+5.4
Stainless-Steel-455	2 313	4.00	-3.35	0.77	71.00	2 880	2 308	+1.8

Table 6. Optimal designs for two-disk compound flywheel with inner and the outer disks made of different materials.



Material	$\omega_d$ (rad/s)	Case 2: $\bar{\omega} = \omega_d$					
		$\alpha_1$	$\alpha_2$	$\beta_2$	$e_m$ (kJ/kg)	$\omega_1$ (rad/s)	$\omega_2$ (rad/s)
Inner: Al-6061-T6	2 171	1.48	4.00	0.95	80.24	2 171	2 171
Outer: Stainless-Steel-455							

4.3.1. Optimization results for single-disk flywheels

Table 3 presents the results obtained by solving the optimization problems defined by Eqs. (37) and (38). The results show that, when the value of  $\bar{\omega}$  is allowed to vary (case 1), the hyperbolic disk geometry yields  $e_m$  values at least 14.3 % higher than those for the uniform disk, as shown in Table 2. The optimized geometry involves values of  $\alpha$  that reach the lower limit ( $\alpha = -4$ ), indicating a rapid tapering of the flywheel’s shape from the inner to the outer surface. As expected, the optimized geometry is the same for all materials. In case 2, where the values of  $\bar{\omega}$  were set to be equal to  $\omega_d$  in Table 2, the optimization produces  $e_m$  values that are modestly increased from those in Table 2 (see case 2 in Table 3) owing to the divergent profile of the optimized geometry ( $\alpha > 0$ ). The results in case 2 support the acceptability of the equations in this paper, being consistent with the results of Kale and Secanell [9] for the same designed rotational speed.

4.3.2. Optimization results for two-disk compound flywheel

Tables 4 and 5 show the optimization results for compound flywheels obtained using Eqs. (39) and (40). The values of  $\omega_1$  and  $\omega_2$  in the tables represent the maximum angular velocities at which the inner and outer disks can operate without failure (with the actual speed limit being the lower of the two values). For optimization case 1, with unconstrained operating speed, the compound flywheel with hyperbolic disks achieves higher values of  $e_m$  compared with equivalent cases in Table 2. For case 2, the values of  $e_m$  are similar to those in Table 2. Also, the values of both  $\alpha_1$  and  $\alpha_2$  reach the upper limit ( $\alpha = +4$ ), so that the geometry involves divergent disks for both the inner and outer parts of the flywheel.

Table 7. Optimal designs for specified maximum rotational speeds of flywheel made of Steel-4340.

$\bar{\omega}$ (rad/s)	Single-disk flywheel			Compound flywheel					Difference (%)	
	$\alpha$	$e_m$ (kJ/kg)		$\alpha_1$	$\alpha_2$	$\beta_2$	$e_m$ (kJ/kg)	$\bar{\omega}_1$ (rad/s)		$\bar{\omega}_2$ (rad/s)
1 100	4.00	18.91		4.00	4.00	0.98	21.56	1 172	1 098	+14.0
1 150	3.05	19.59		4.00	4.00	0.96	23.22	1 193	1 148	+18.5
1 196	2.04	20.41		4.00	4.00	0.93	24.15**	1 250	1 193	+18.3
1 250	1.01	21.32		4.00	-0.80	0.81	22.59	1 493	1 248	+5.9
1 294	0.25	22.02		4.00	-3.65	0.77	22.25	1 602	1 291	+1.1
1 300	0.14	22.12		4.00	-3.96	0.76	22.24	1 615	1 297	+0.5
1 350	-0.67	22.87		4.00	-3.93	0.70	21.64	1 787	1 348	-5.4
1 400	-1.45	23.56		4.00	-4.00	0.65	21.35	1 937	1 398	-9.4
1 450	-2.20	24.19		4.00	-4.00	0.61	21.22	2 083	1 147	-12.3
1 500	-2.95	24.77		4.00	-4.00	0.58	21.21	2 254	1 497	-14.4
1 550	-3.72	25.28		-	-	-	-	-	-	-
1 566	-4.00	26.61**		-	-	-	-	-	-	-

When comparing the results from case 1 for the single-disk and compound flywheels, it can be seen that the maximum values of  $e_m$  obtained with the compound flywheels are lower for all designs. Furthermore, the rotational speed that yields the maximum  $e_m$  is also lower for the compound flywheels. This may be attributed to the effect of contact stress associated with interference fitting of the parts.

As previously noted [9, 13], the maximum value of  $e_m$  for a compound flywheel can be increased by selecting different materials for the inner and outer parts of flywheel. For this case, the materials are chosen independently for each part of flywheel and the shape optimization is based on Eq. (41). The results show that the highest value of  $e_m$  can be achieved when the inner and outer part of flywheel are made of Al-7075-T6 and Stainless-Steel-455 respectively, and the maximum  $e_m$  value can be increased to 80.24 kJ/kg, as presented in Table 6.

4.3.3. Optimization results for specified maximum rotational speed

Table 7 presents the optimization results obtained for Steel-4340 material, considering a range of designated maximum rotational speeds. Superscripts (\*\*) in the table indicate the maximum specific energy  $e_m$  that can be achieved for each type of flywheel. These values are computed by solving the optimization problems defined by Eqs. (38) and (40). The optimized values are 26.61 kJ/kg for single-disk flywheel and 24.15 kJ/kg for compound flywheel, corresponding to maximum operating speeds of 1 566 and 1 196 rad/s, respectively.

The optimized values of  $e_m$  in Table 7, are plotted in Fig. 8 as a function of maximum rotational speed, for both single-disk and compound flywheels. The figure shows that, for lower operating speeds ( $\omega_d < 1300$  rad/s), the compound flywheel has significantly more potential for generating high  $e_m$  than the single-disk flywheel. On the other hand, for higher designed designated speeds ( $\omega_d > 1300$  rad/s), the values of  $e_m$  obtained with an optimized single-disk flywheel are greater than those for the compound flywheel. Regarding the compound flywheel, there is no design solution that allows the inner and outer disks to have the same failure speed. This limitation arises from the design constraints. However, within a range of operating speed (between 1150 and 1196 rad/s) where the designed compound flywheels provide high  $e_m$  values, the failure speeds of the inner and outer disks are closest.

It is also observed that, for maximum operating speeds greater than 1500 rad/s, there is no feasible design solution for the compound rotor. The reason for this may be explained by Fig. 9 which presents the relationship between  $\beta_2$  and  $e_m$  of compound flywheel. The figure shows that the value of  $\beta_2$ , which is related to  $r_m$ , decreases gradually when the rotation speed increases. This implies that to obtain the maximum values of  $e_m$  at higher speed, the region of external rotor of compound flywheel needs to be



expanded. Since the values of  $\beta_2$  cannot be lower than 0.55 ( $r_{i2} = r_m \sim r_{i1}$ ), Eq. (40) cannot produce physically meaningful solutions when the designed operating speed is greater than 1500 rad/s.

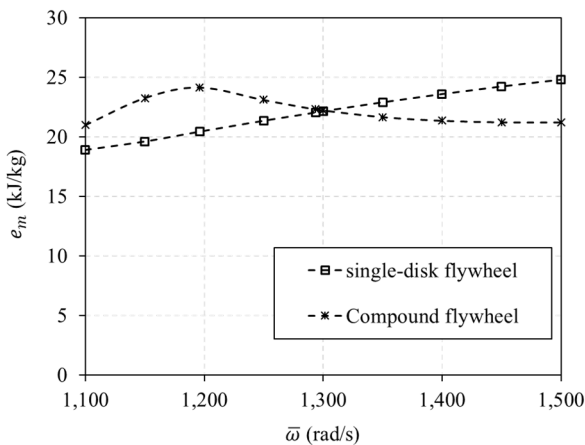


Fig. 8. The specific energy  $e_m$  of flywheels optimized for different maximum rotational speeds.

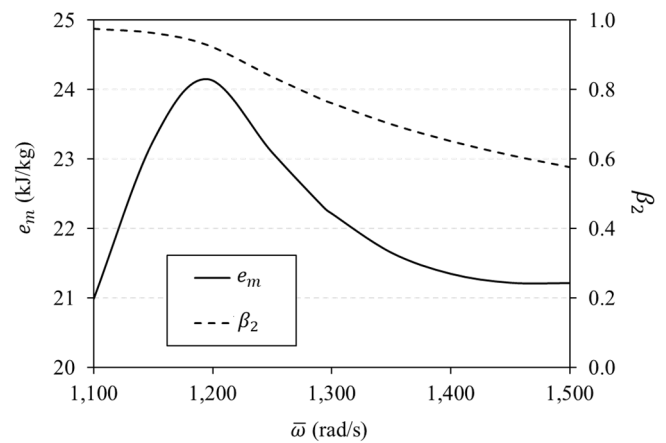


Fig. 9. The values of  $e_m$  and  $\beta_2$  obtained by solving Eq. (40) with different prescribed maximum speeds.

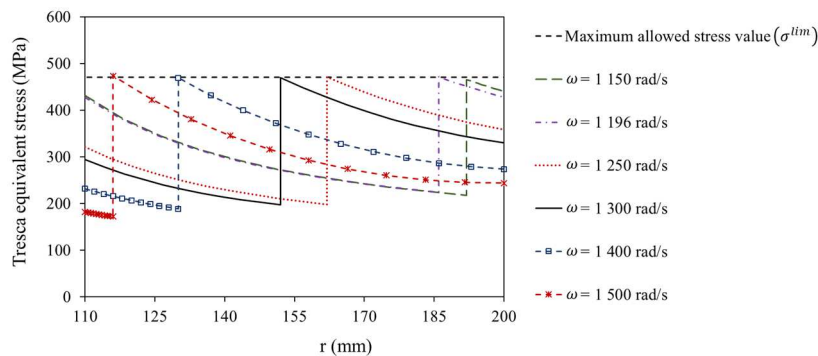


Fig. 10. Tresca equivalent stress in compound flywheels optimized for various designed maximum speeds.

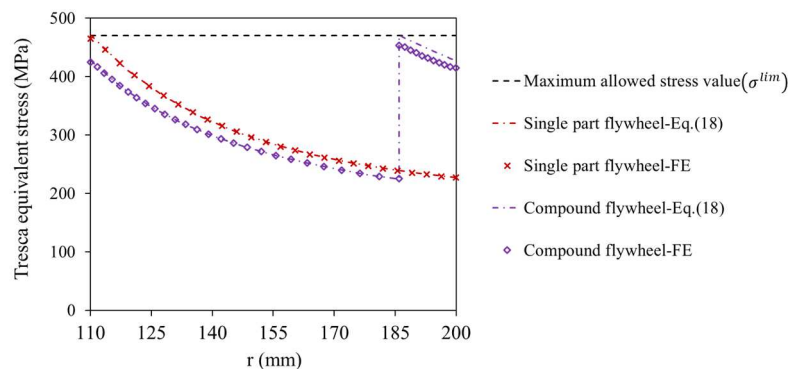


Fig. 11. The Tresca equivalent stress in optimized flywheels having designed maximum speed of 1196 rad/s.

#### 4.3.4. Stress distribution

Figure 10 illustrates the Tresca equivalent stress evaluated as a function of radius for the optimized compound flywheels selected from Table 7. The figure reveals that, for the rotors designed to operate at maximum speeds between 1 150 and 1 196 rad/s, the stress at the inner surface of both the inner and outer disks approaches the limiting stress  $\sigma^{lim}$ . This matches the unconstrained optimality conditions previously described in Section 3. However, in cases with a maximum rotational speed higher than 1 196 rad/s, the stress occurring at the inner surface of the inner disk is significantly lower than  $\sigma^{lim}$ . Therefore, if the geometric parameters were unconstrained, there would be remaining design freedom that could be used to increase the moment of inertia. To achieve this, the allowed range for the design variables,  $\alpha_1$  and  $\alpha_2$ , must be expanded. However, this would lead to an optimized geometry that may be less practical for manufacture.

Figures 11 shows the Tresca equivalent stress along the radial direction for the single-disk and compound flywheels having a failure speed of 1 196 rad/s. The stress variations in this figure are computed using Eq. (18), and the optimization results in Table 7. The optimized geometries involve  $\alpha = 2.04$ ,  $\beta = 0.55$  for the single-disk flywheel and  $\alpha_1 = 4.00$ ,  $\alpha_2 = 4.00$ ,  $\beta_2 = 0.93$  for the compound



flywheel. The figure shows that the stress in the compound flywheel is close to  $\sigma^{\text{lim}}$  at the inner surface of both the inner and outer disk. This differs from the case of a single-disk flywheel, for which the stress reaches  $\sigma^{\text{lim}}$  at only one radial position: the disk inner surface. In simple terms, the compound flywheel can provide higher values of  $e_m$  because the stress developed in the compound flywheel is more uniform than in the single-disk flywheel.

4.3.5. Effect of mass ratio ( $\eta$ )

Table 10 shows results obtained for the compound flywheel design optimization with various fixed values of mass ratio ( $\eta = m_2 / m_1$ ). The data in the table is for optimized flywheels having a designed maximum rotational speed of 1 196 rad/s. The results show that changing the value of  $\eta$  has little effect on the optimized parameter values ( $\alpha_1, \alpha_2$  and  $\beta_2$ ). According to Eqs. (39)-(40), although  $\eta$  does not greatly influence the optimized geometric parameters, it does have a direct impact on the optimized value of  $e_m$ , which increases with the value of  $\eta$ . For example, the compound flywheel with  $\eta = 8$  will provide the value of  $e_m$  about 26.4% higher than for the single-disk flywheel. The relation between  $e_m$  and  $\eta$  is also plotted in Fig. 12. The figure shows that the optimized value of  $e_m$  tends to a constant as the value of  $\eta$  increases. This is because the second term in Eqs. (39) and (40), which involves the inertia of the outer disk, becomes dominant for large  $\eta$ .

Table 10. Optimal designs with different mass ratio  $\eta = m_2 / m_1$ .

$\bar{\omega}$ (rad/s)	Single-disk flywheel		Compound flywheel					Difference (%)
	$\alpha$	$e_m$ (kJ/kg)	$\alpha_1$	$\alpha_2$	$\beta_2$	$e_m$ (kJ/kg)	$\eta$	
1 196	2.04	20.41	4.00	4.00	0.93	20.55	0.25	+ 0.7
			4.00	4.00	0.93	21.58	0.50	+ 5.7
			4.00	4.00	0.93	22.87	1.00	+ 12.0
			4.00	4.00	0.93	24.15	2.00	+ 18.3
			4.00	4.00	0.93	25.16	4.00	+ 23.3
			4.00	4.00	0.93	25.86	8.00	+ 26.4

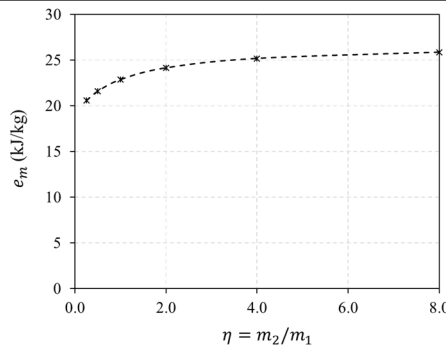


Fig. 12. The effect of disk mass ratio  $\eta$  on specific energy.

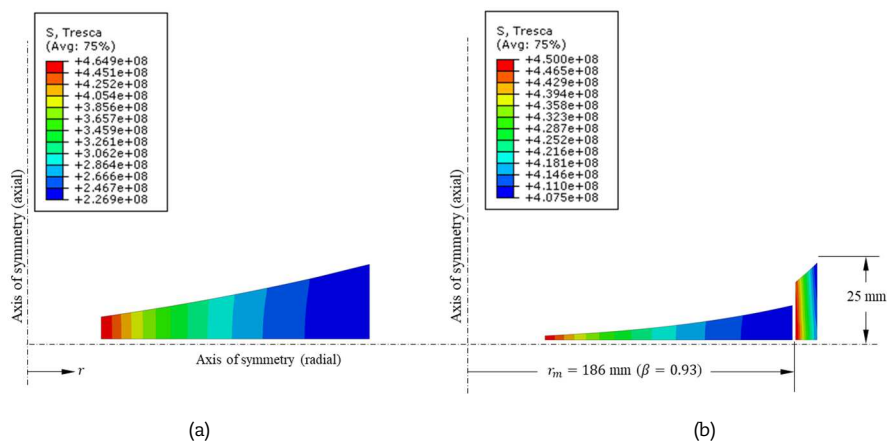


Fig. 13. Tresca equivalent stress developed in flywheels having designed maximum speed of 1 196 rad/s;

(a) single-disk flywheel and (b) compound flywheel with  $\eta = 2$ .

4.3.6. Finite element (FE) simulation and model validation

To verify the results obtained from the optimization procedures, FE models for the single-disk and compound flywheels were established in ABAQUS [29]. Owing to symmetry, the model involves only a single quadrant of the flywheel. The 4-node bilinear axisymmetric quadrilateral element, and reduced integration (CAX4R) method were used throughout. The FE analysis is composed of two main steps. First, the flywheel parts are subjected to the inner and outer contact pressures (where present). In the second step, the rotational body force is applied to the model in small increments until it matches the designated. The main result of interest is the variation of Tresca equivalent stress along the middle radial axis of the flywheels. These results are presented in Fig. 9 for flywheels optimized for a maximum designated speed of 1 196 rad/s. It can be seen that the FE-results agree well with the analytical results from Eq. (18), and differences are within a few percent.



Figure 13 shows the distribution of Tresca equivalent stress throughout the FE models for both the single-disk and compound flywheel made of Steel-4340. The figure shows that the stress fields developed in the innermost disk of the flywheels are quite uniform along the axial direction. This is consistent with the assumption of having no stress variation in the axial direction, as previously adopted in the theory of Section 2.

For the stress distribution in the outer disk of the compound flywheel (Fig. 13b), there is a more significant axial variation. This is partly due to the finite axial length of the contact zone with the inner disk. Although this situation differs from the conditions used to develop the theory in Section 2 (which assumed that the disk is subject to uniform pressure over the inner surface), the peak values of stress occur along the radial symmetry axis. Therefore, the values of stress obtained using Eq. (18) agree closely with the peak values obtained from the FE simulations. Moreover, the values of Tresca equivalent stress occurring along the radial symmetry axis are higher than the stresses in other areas, and so the proposed analytical equations can be validly used in design optimization problems for compound flywheel rotors.

## 5. Conclusions

The mathematical formulation and solution of parametric shape optimization problems in the design of flywheel rotors to maximize energy storage capacity is both challenging and practically important. In this paper, a solution method has been proposed for the case of a multi-layer flywheel, assembled by press fitting or bonding of concentric rotor parts. Explicit formulae have been defined for cases with annular hyperbolic disks that show the influence of key parameters on the stress fields due to centrifugal loading and interfacial pressures. The study also reveals some important underlying concepts for solving these types of problems: namely, the utilization of multiplicative factors that separately account for the stress and mass distributions within the definitions of the shape optimization problem.

The case studies, focusing on single and two-disk rotor designs, confirm the effectiveness and validity of the proposed approach. The findings highlight that compound rotor flywheels can achieve markedly higher energy storage capacities, compared to single-disk designs, for cases with lower operational speeds. This underlines the substantial role of compound rotor shape optimization in the overall design process of flywheels. For future research, the following directions are proposed:

- Application of the proposed design optimization framework to a wider range of materials and geometries, broadening the scope of flywheel technology.
- Experimental validation and testing of the optimized flywheel designs in real-world settings to further assess their practical viability and performance under various operational conditions.
- Integration of advanced materials and manufacturing methods to explore the limits of energy storage efficiency and operational stability in flywheel systems.

In conclusion, the methodologies developed in this paper hold significant potential for advancing the design of cost-effective and high-performance flywheel systems, offering a valuable contribution to the field of energy storage technology.

## Author Contributions

Sutham Arun played a role in conceptualization, methodology, developing the mathematical model, interpreting the results, validation, formal analysis, and partially writing the manuscript; Matthew Cole played a role in conceptualization, methodology, developing mathematical model, interpreting the results, formal analysis and partially writing the manuscript; Wichaphon Fakkaew played a role in interpreting the mathematical results, formal analysis, and visualization; Chakkapong Chamroon played a role in revising the manuscript and investigation. The manuscript was written through the contribution of all authors. All authors discussed the results, reviewed, and approved the final version of the manuscript.

## Acknowledgments

Not applicable.

## Conflict of Interest

The authors declared no potential conflicts of interest concerning the research, authorship, and publication of this article.

## Funding

Financial support of this work was provided by the Fundamental Fund of University of Phayao (Agreement FF65-RIM078).

## Data Availability Statements

For the case studies presented in Section 4, the optimization results were obtained using the built-in evolutionary algorithm (EA) solver in Microsoft Excel. All information, including the Excel spreadsheet files, is provided by the authors as supplementary data. This can be used to reproduce the results in the paper.

## Nomenclature

$c_e$	Shape factors that quantify the impact of external pressure on Tresca stress	$\beta$	Ratio of the inner radius to the outer radius
$c_i$	Shape factors that quantify the impact of internal pressure on Tresca stress	$\gamma$	Material density [kg/m <sup>3</sup> ]
$\bar{E}_k$	Kinetic energy [kJ]	$\eta$	Mass ratio
$e_m$	Specific energy [kJ/kg]	$\rho$	Ratio of the radial distance to the outer radius
$h$	Disk thickness [m]	$\kappa_\omega$	Shape factors that quantify the impact of centrifugal force on Tresca stress
		$\kappa^J$	Shape factor accounting for the mass distribution



$r_e$	Outer radius [m]	$\kappa^\sigma$	Shape factor accounting for the stress distribution
$r_i$	Inner radius [m]	$\sigma^{\text{lim}}$	Allowable stress [N/m <sup>2</sup> ]
$K$	Overall shape factor	$\bar{\omega}$	Maximum permitted angular velocity [rad/s]
$m$	Mass [kg]	$\omega_d$	Specified angular velocity [rad/s]
$V$	Volume [m <sup>3</sup> ]		
$\alpha$	The constant defined to characterize hyperbolic profile		

## Appendix

The stresses and the radial displacement due to centrifugal load  $\sigma_o$  are:

$$(\sigma_r)_\omega = (3 + \nu) \frac{\left[ (\beta^2 - \beta^{q-1}) \rho^{p-1} + (\beta^{p-1} - \beta^2) \rho^{q-1} - (\beta^{p-1} - \beta^{q-1}) \rho^2 \right]}{[8 + (3 + \nu)\alpha](\beta^{p-1} - \beta^{q-1})} \sigma_o \quad (\text{A.1})$$

$$(\sigma_t)_\omega = \frac{\left[ -q(3 + \nu)(\beta^2 - \beta^{q-1}) \rho^{p-1} - p(3 + \nu)(\beta^{p-1} - \beta^2) \rho^{q-1} - (1 + 3\nu)(\beta^{p-1} - \beta^{q-1}) \rho^2 \right]}{[8 + (3 + \nu)\alpha](\beta^{p-1} - \beta^{q-1})} \sigma_o \quad (\text{A.2})$$

$$u_\omega = \frac{r_e}{E} \frac{\left[ -(q + \nu)(3 + \nu)(\beta^2 - \beta^{q-1}) \rho^p - (p + \nu)(3 + \nu)(\beta^{p-1} - \beta^2) \rho^q - (1 - \nu^2)(\beta^{p-1} - \beta^{q-1}) \rho^3 \right]}{[8 + (3 + \nu)\alpha](\beta^{p-1} - \beta^{q-1})} \sigma_o \quad (\text{A.3})$$

The stresses and the radial displacement due to the pressure acting on the disk outer surface  $\sigma_e$  are:

$$(\sigma_r)_e = \frac{(\beta^{p-1} \rho^{q-1} - \beta^{q-1} \rho^{p-1})}{(\beta^{p-1} - \beta^{q-1})} \sigma_e \quad (\text{A.4})$$

$$(\sigma_t)_e = \frac{(q \beta^{q-1} \rho^{p-1} - p \beta^{p-1} \rho^{q-1})}{(\beta^{p-1} - \beta^{q-1})} \sigma_e \quad (\text{A.5})$$

$$u_e = \frac{r_e}{E} \frac{(q + \nu) \beta^{q-1} \rho^p - (p + \nu) \beta^{p-1} \rho^q}{(\beta^{p-1} - \beta^{q-1})} \sigma_e \quad (\text{A.6})$$

The stresses and the radial displacement due to the pressure acting on the disk inner surface  $\sigma_i$  are:

$$(\sigma_r)_i = \frac{(\rho^{p-1} - \rho^{q-1})}{(\beta^{p-1} - \beta^{q-1})} \sigma_i \quad (\text{A.7})$$

$$(\sigma_t)_i = \frac{(-q \rho^{p-1} + p \rho^{q-1})}{(\beta^{p-1} - \beta^{q-1})} \sigma_i \quad (\text{A.8})$$

$$u_e = \frac{r_e}{E} \frac{(p + \nu) \rho^q - (q + \nu) \rho^p}{(\beta^{p-1} - \beta^{q-1})} \sigma_i \quad (\text{A.9})$$

## References

- [1] Pullen, K.R., The status and future of flywheel energy storage, *Joule*, 3, 2019, 1394-1399.
- [2] Arabkoohsar, A., *Mechanical energy storage technologies*, Academic Press: London, London, 2020.
- [3] Krack, M., Secanell, M., Mertiny, P., Cost optimization of hybrid composite flywheel rotors for energy storage, *Structural and Multidisciplinary Optimization*, 41, 2010, 779-795.
- [4] Dragoni, E., Mechanical design of flywheels for energy storage: A review with state-of-the-art developments, *Proceedings of the Institution of Mechanical Engineers, Part L: Journal of Materials: Design and Applications*, 233(5), 2019, 995-1004.
- [5] Mousavi, G.S.M., Faraji, F., Majazi, A., Al-Haddad, K., A comprehensive review of Flywheel Energy Storage System technology, *Renewable and Sustainable Energy Reviews*, 67, 2017, 477-490.
- [6] Krack, M., Secanell, M., Mertiny, P., Advanced optimization strategies for cost-sensitive design of energy storage flywheel rotors, *Journal of Advanced Materials*, 43(2), 2011, 65-78.
- [7] Krack, M., Secanell, M., Mertiny, P., Cost optimization of a hybrid composite flywheel rotor with a split-type hub using combined analytical/numerical models, *Structural and Multidisciplinary Optimization*, 43, 2011, 57-73.
- [8] Ha, S.K., Kim, D.J., Sung, T.H., Optimum design of multi-ring composite flywheel rotor using a modified generalized plane strain assumption, *International Journal of Mechanical Sciences*, 43(4), 2001, 993-1007.
- [9] Kale, V., Secanell, M., A comparative study between optimal metal and composite rotors for flywheel energy storage systems, *Energy Reports*, 4, 2018, 576-585.
- [10] Li, X., Mittelstedt, C., Binder, A., A review of critical issues in the design of lightweight flywheel rotors with composite materials, *e + i Elektrotechnik und Informationstechnik*, 139, 2022, 204-221.



- [11] Kale, V., Thomas, M., Secanell, M., On determining the optimal shape, speed, and size of metal flywheel rotors with maximum kinetic energy, *Structural and Multidisciplinary Optimization*, 64, 2021, 1481-1499.
- [12] Arslan, M.A., Flywheel geometry design for improved energy storage using finite element analysis, *Materials and Design*, 29(2), 2008, 514-518.
- [13] Genta, G., *Kinetic Energy Storage: Theory and practice of advanced flywheel systems*, Butterworth-Heinemann, London, 1985.
- [14] Janse van Rensburg, P.J., Groenwold, A.A., Wood, D.W., Optimization of cylindrical composite flywheel rotors for energy storage, *Structural and Multidisciplinary Optimization*, 47, 2013, 135-147.
- [15] Dongxu, H., Xingjian, D., Wen, L., Yangli, Z., Xuehui, Z., Haisheng, C., Zhilai, Z., A review of flywheel energy storage rotor materials and structures, *Journal of Energy Storage*, 74(A), 2023, 109076.
- [16] Kress, G., Shape optimization of a flywheel, *Structural and Multidisciplinary Optimization*, 19, 2000, 74-81.
- [17] Vullo, V., Vivio, F., *Rotors: Stress analysis and design*, Springer: London, London, 2013.
- [18] Vivio, F., Vullo, V., Cifani, P., Theoretical stress analysis of rotating hyperbolic disk without singularities subjected to thermal load, *Journal of Thermal Stresses*, 37, 2013, 117-136.
- [19] Vullo, V., Vivio, F., Elastic stress analysis of non-linear variable thickness rotating disks subjected to thermal load and having variable density along the radius, *International Journal of Solids and Structures*, 45(10), 2008, 5337-5355.
- [20] Mack, W., Rotating elastic-plastic tube with free end, *International Journal of Solids and Structures*, 27(11), 1991, 1461-1476.
- [21] Prokudin, A., Schmidt-Ishlinskii yield criterion and a rotating cylinder with a rigid inclusion, *Journal of Applied and Computational Mechanics*, 7(2), 2021, 858-869.
- [22] Nejad, M.Z., Fatehi, P., Exact elasto-plastic analysis of rotating thick-walled cylindrical pressure vessels made of functionally graded materials, *International Journal of Engineering Science*, 86, 2015, 26-43.
- [23] Zenkour, A.M., Mashat, D.S., Stress function of a rotating variable-thickness annular disk using exact and numerical methods, *Engineering*, 3, 2011, 422-430.
- [24] Sebastian, R., Pena Alzola, R., Flywheel energy storage systems: Review and simulation for an isolated wind power system, *Renewable and Sustainable Energy Reviews*, 16, 2012, 6803-6813.
- [25] Srinivasan, P., Rotating disc with a stress-variation given by unit function, *Journal of the Indian Institute of Science*, 36, 1954, 88-94.
- [26] Stodola, A., Lowenstein, L.C., *Steam and gas turbines with a supplement on the prospects of the thermal prime mover*, Peter Smith, New York, 1945.
- [27] Vikhar, P.A., Evolutionary algorithms: A critical review and its future prospects, *Proceedings of the 2016 International Conference on Global Trends in Signal Processing, Information Computing and Communication (ICGTSPICCC)*, 261-265, 2016.
- [28] Adam, S., Halina, K., Evolutionary algorithms and their applications to engineering problems, *Neural Computing and Applications*, 32, 2020, 12363-12379.
- [29] Dassault Systemes Simulia Crop, *ABAQUS Analysis User's Manual*, Rhode Island, USA, 2022.

## ORCID iD

Sutham Arun  <https://orcid.org/0000-0002-7899-6691>  
 Wichaphon Fakkaew  <https://orcid.org/0000-0001-6812-2088>  
 Chakkapong Chamroon  <https://orcid.org/0000-0003-3174-841X>  
 Matthew Owen Thomas Cole  <https://orcid.org/0000-0002-1157-6537>



© 2024 Shahid Chamran University of Ahvaz, Ahvaz, Iran. This article is an open access article distributed under the terms and conditions of the Creative Commons Attribution-NonCommercial 4.0 International (CC BY-NC 4.0 license) (<http://creativecommons.org/licenses/by-nc/4.0/>).

**How to cite this article:** Arun S., Fakkaew W., Chamroon C., Cole M.O.T. On the Energy Storage Capacity and Design Optimization of Compound Flywheel Rotors with Prestressed Hyperbolic Disks, *J. Appl. Comput. Mech.*, xx(x), 2024, 1-16. <https://doi.org/10.22055/jacm.2024.45770.4412>

**Publisher's Note** Shahid Chamran University of Ahvaz remains neutral with regard to jurisdictional claims in published maps and institutional affiliations.

